

Planar electrical-substitution carbon nanotube cryogenic radiometer

This content has been downloaded from IOPscience. Please scroll down to see the full text.

2015 Metrologia 52 376

(<http://iopscience.iop.org/0026-1394/52/2/376>)

View [the table of contents for this issue](#), or go to the [journal homepage](#) for more

Download details:

IP Address: 132.163.53.72

This content was downloaded on 31/03/2015 at 15:19

Please note that [terms and conditions apply](#).

Planar electrical-substitution carbon nanotube cryogenic radiometer*

N A Tomlin¹, M White¹, I Vayshenker¹, S I Woods² and J H Lehman¹

¹ National Institute of Standards and Technology (NIST), Boulder, CO 80305, USA

² National Institute of Standards and Technology (NIST), Gaithersburg, MD 20899, USA

E-mail: nathan.tomlin@nist.gov

Received 18 November 2014, revised 28 January 2015

Accepted for publication 30 January 2015

Published 30 March 2015



Abstract

We have developed a fully-lithographic electrical-substitution planar bolometric-radiometer (PBR) that employs multiwall vertically-aligned carbon nanotubes (VACNT) as the absorber and thermistor, micro-machined Si as the weak thermal link and thin-film Mo as the electrical heater. The near-unity absorption of the VACNT over a broad wavelength range permits a planar geometry, compatible with lithographic fabrication. We present performance results on a PBR with an absorption of 0.99935 at 1550 nm, a thermal conductance of $456 \mu\text{W K}^{-1}$ at 4 K and a time constant ($1/e$) of 7.7 ms. A single measurement of approximately 100 μW optical power at 1550 nm achieved in less than 100 s yields an expanded uncertainty of 0.14% ($k = 2$). We also observe an elevated superconducting transition temperature of 3.884 K for the Mo heater, which opens the possibility of future devices incorporating more sensitive thermistors and superconducting thin-film wiring.

Keywords: electrical-substitution, cryogenic radiometer, bolometer, vertically-aligned carbon nanotubes, optical fiber, optical power

(Some figures may appear in colour only in the online journal)

1. Introduction

Since 1985, electrical-substitution radiometers (ESRs) have served as primary standards for optical power at national metrology institutes around the world [1]. In order to accurately measure optical power, ESRs are designed to absorb as close to 100% of incident optical power as possible. To achieve the necessary near-unity absorption, nonideal optical absorbers require a trap or cavity design for multiple reflections. The resulting macroscopic cavity limits the minimum size and therefore the minimum time constant of a radiometer. While cavities can be miniaturized [2, 3], cavity-based hand-assembled radiometers are labor-intensive to assemble and difficult to reproduce.

Vertically-aligned carbon nanotubes (VACNT) have been shown to be the most ideal absorber known [4–8]. The absorption of VACNT is high enough that for many applications, a cavity is unnecessary. A planar VACNT absorber allows for lithographic fabrication, which has many benefits, including low cost, simple to duplicate or systematically modify and no labor-intensive assembly required.

* Contribution of an agency of the US government; not subject to copyright

We have developed a fully-lithographic carbon nanotube planar bolometric-radiometer (PBR) designed for cryogenic electrical-substitution measurements of optical fiber power. All ESRs require 4 components: a weak thermal link, thermometer, optical absorber and electrical heater. On the PBR, the weak thermal link is provided by a micro-machined Si leg, the thermometer and optical absorber are multiwall VACNT and the electrical heater is thin-film Mo. As a demonstration of the versatility of the lithographic design, the PBR has been designed to be compatible with the low background infrared (LBIR) facility at NIST Gaithersburg [9]. The absorber area is compatible with the free space beam size, the thermal conductance is designed for typical applied powers and the heater and thermistor resistances are matched to existing cryogenic radiometer readout electronics. Results from the LBIR facility will be presented in a future paper.

We have previously reported on an initial proof-of-principle device [10], however, the current PBR improves upon the previous design in several areas: thin-film Mo for the electric heater and thermistor contacts, reduced size and wirebonds for

electrical contact. In addition, we present measurement results that demonstrate uncertainty and equivalence as it pertains to the accuracy of the PBR and its use as a primary standard.

2. Fabrication and design

Multiple PBRs were fabricated on a 76.2 mm diameter double-side polished silicon wafer. Thermal SiO_2 was grown on both sides of the wafer to a thickness of 415 nm. Molybdenum was sputter deposited to 53 nm on one side (hereafter referred to as the frontside of the wafer). The Mo was then lithographically patterned with 1 μm photoresist and wet-etched using Al etchant. After the photoresist was stripped using acetone, the SiO_2 was removed from the backside of the wafer with a reactive ion etch (RIE). The frontside was lithographically patterned with 1 μm photoresist and then shipped to a commercial nanotube company for deposition of VACNT catalyst, which consisted of electron beam deposition of 20 nm Al_2O_3 followed by 2 nm Fe. The wafer was then shipped back to NIST for further processing. The wafer was exposed to ultrasound in acetone to strip the photoresist and lift-off the catalyst layers. The frontside was lithographically patterned with 7 μm photoresist and exposed to a RIE to remove the SiO_2 . Wax was then used to attach the Si wafer to a sapphire backing wafer, followed by deep RIE using a Bosch process plasma etch to micro-machine the Si and define the PBR geometry. The photoresist was stripped by exposure to oxygen plasma, followed by ultrasound in acetone, which also released the Si wafer from the sapphire wafer. The Si wafer was then shipped back to the nanotube company for water-assisted chemical vapor deposition of VACNT.

The multiwall VACNT growth process was performed in a 130 mm inner diameter tube furnace. All steps were conducted at atmospheric pressure (101.3 kPa) with a constant flow of 2800 sccm N_2 . The furnace was first ramped to 650 $^\circ\text{C}$ over 15 min. Catalyst ‘seasoning’ (formation of islands) was accomplished by flowing H_2 at 195 sccm for 15 min. The furnace was then ramped to 780 $^\circ\text{C}$ over 5 min. VACNT growth was initiated by flowing C_2H_4 at 100 sccm along with N_2 at 80 sccm through a H_2O bubbler for 15 min. After growth, the gas flows of H_2 , C_2H_4 and N_2 bubbler were all stopped and the furnace was cooled to 250 $^\circ\text{C}$ before opening. The finished wafer was then shipped back to NIST.

Figure 1 shows a finished wafer with PBR variations for the thermal link, thermistor and thin-film heater. Individual chips were removed from the wafer by being forced to flex out of the wafer plane, until the Si cleaved at two weak attachment points. The center 10 mm by 10 mm chip is a witness sample for measuring the VACNT reflectance.

Each PBR has a 4 mm by 10 mm base with two 1.575 mm diameter holes (for English #0–80 screws) for attachment to a heatsink. A single Si leg 1.94 mm long, 233 μm wide and 375 μm thick supports the radiometer main body that holds the thermistor, optical absorber and electrical heater (figure 2(a)). VACNT grow only over areas with catalyst and grow equally well over SiO_2 and Mo underlayers (figure 2(b)) [11, 12]. The base of the VACNT thermistor is 300 μm by 1000 μm and

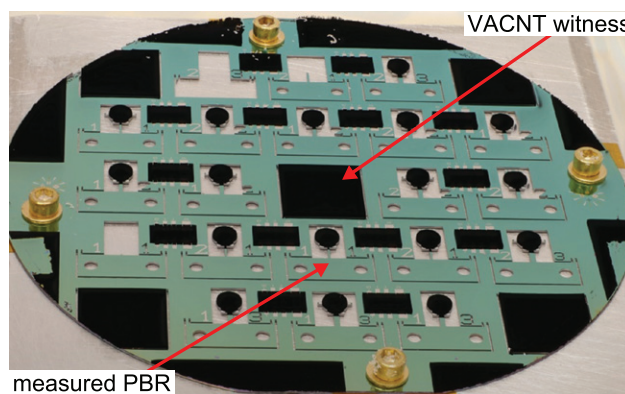


Figure 1. Finished wafer with multiple PBRs. Red arrows show the PBR and witness sample measured for this paper.

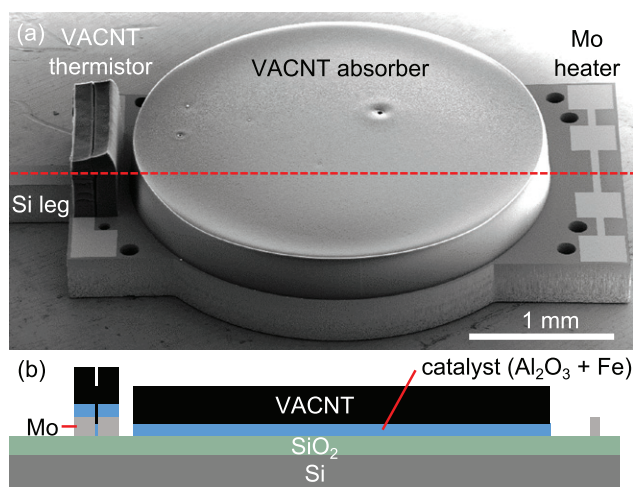


Figure 2. (a) Scanning electron microscope (SEM) image of main body of a PBR (different from device measured in this paper). (b) Schematic sectional view of red dashed cut line in (a). Thicknesses are not to scale.

electrical contact is accomplished by Mo leads with a rectangular area between the leads of 100 μm by 1000 μm . The base of the VACNT optical absorber is a 3 mm diameter circle. The Mo electrical heater is 50 μm by 900 μm with 4 larger areas for bondpads. The 8 small holes in the radiometer main body are not used.

Using a digital contact sensor attached to the vertical axis of an optical microscope, we measured the VACNT height to be 275 μm to 285 μm over SiO_2 and 308 μm to 355 μm over Mo. We are currently investigating the underlayer-dependent growth rate. We note that we have observed the opposite affect (growth rate higher over SiO_2 than Mo) on a separate wafer, which suggests the different growth rates are not inherent to the underlayer material, but are instead dependent on the specific surface preparations and growth conditions.

3. Measurement setup

The PBR is attached to a Cu mount using two #0–80 screws with washers (figure 3). Electrical contact between the PBR Mo bondpads and the Cu traces on a surrounding printed circuit board (PCB) is made by eight Al (with 1% Si) wirebonds

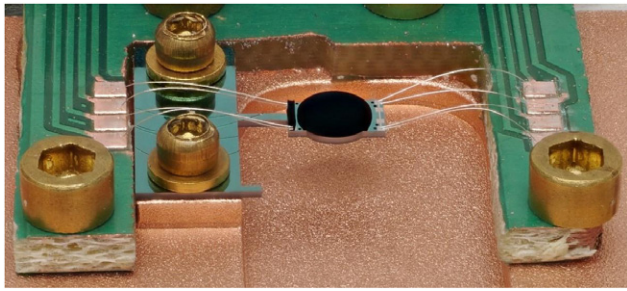


Figure 3. PBR attached to Cu mount and wirebonded to PCB.

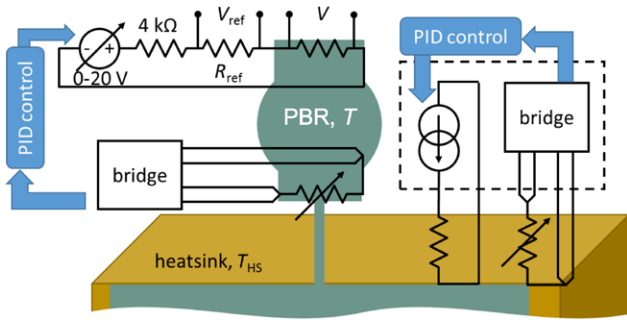


Figure 4. Schematic of electrical measurement showing PID temperature control loops for both the heatsink and PBR.

with dimensions approximately 7 mm long and 25.4 μm diameter. The Cu mount is bolted to a larger Cu stage, which has a thermistor and low temperature-coefficient 1 k Ω resistor, both attached with varnish. We will refer to this temperature stage as the heatsink, which provides a temperature-stabilized thermal reservoir to reduce temperature variation experienced by the PBR. The heatsink is attached to the mixing chamber of a dilution refrigerator through five 101.6 mm long, 6 mm diameter stainless steel rods. A resistance bridge is used to control the heatsink temperature by monitoring the thermistor and heating the resistor, using a proportional-integral-derivative (PID) loop (figure 4). A voltage source, low temperature-coefficient current reference resistor and resistance bridge are used to monitor the PBR thermistor and heat the PBR electrical heater, using a PID loop.

Input optical power is coupled to the VACNT using a standard 8.2 μm core, single-mode telecommunication fiber (no anti-reflection coating) with an FC/PC connector that is aligned at normal incidence to the center of the VACNT absorber. The distance between the fiber tip and VACNT is 4.5 mm, which gives a spot size diameter ($1/e^2$) of 846 μm , assuming a beam diameter at the fiber tip of 10.5 μm [13]. Optical power is applied with a 1550 nm continuous wave fiber laser coupled to a programmable fiber attenuator, followed by a fiber switch with port 1 measured by a free-space optical power meter that has been NIST-calibrated and port 2 coupled to the PBR (figure 5(a)). Before and/or after each measurement run, when the cryostat is open to atmosphere, the FC/PC connector is disconnected from the PBR so both fiber ports can be measured with the optical power meter in order to calibrate the switching ratio of the fiber switch (figure 5(b)).

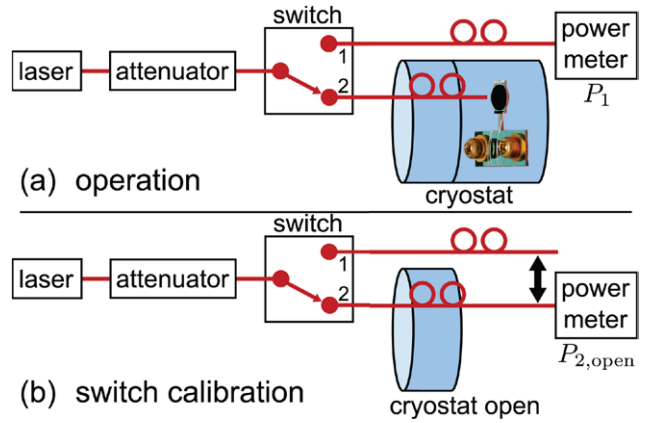


Figure 5. Schematics of optical measurement. (a) Optical setup during operation. (b) Optical setup used to find switching ratio before and/or after operation when cryostat is open.

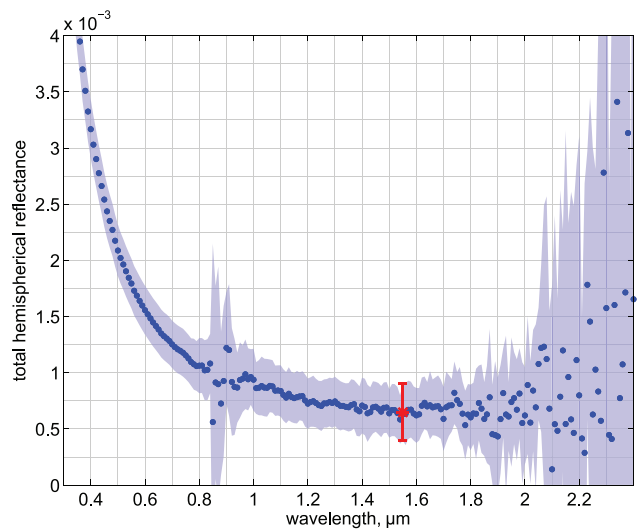


Figure 6. VACNT witness chip total hemispherical reflectance with uncertainty ($k = 2$) shown by shaded region. The reflectance at 1550 nm is shown by a red asterisk with error bars.

4. Absorber

We measured the total hemispherical reflectance (THR) of the witness chip using a spectrophotometer with a 150 mm integrating sphere accessory. The sample was held at the back of the sphere against a 9.5 mm diameter port, the incident light spot size on the sample was 5 mm by 7.2 mm and all other settings were identical to those reported elsewhere [8]. At 1550 nm, the measured total hemispherical reflectance $R_{\text{THR}} = 6.5 \times 10^{-4}$ (figure 6), which corresponds to an absorptance of 0.99935. During VACNT growth on the wafer, the center of the witness chip was 8.9 mm away from the center of the measured PBR absorber (figure 1). We make the assumptions that the reflectances of the VACNT on the witness chip and the PBR are identical and that the reflectance under conditions of atmospheric pressure at 294 K is identical to the reflectance under conditions of vacuum at 4 K. Further studies are needed to test these assumptions, but for the present calculations, we have doubled the measurement uncertainty

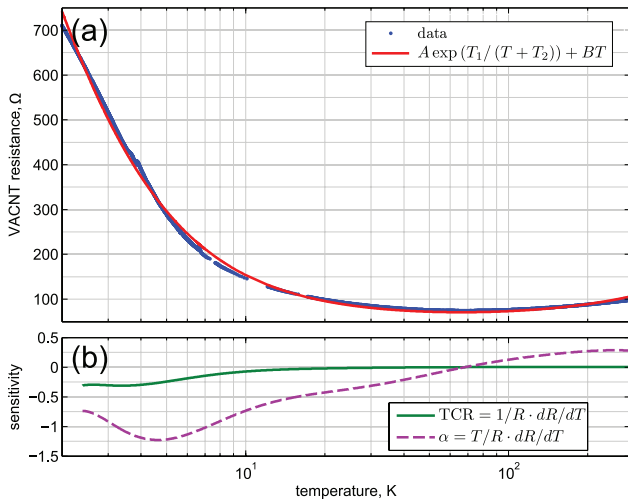


Figure 7. (a) VACNT thermistor resistance as a function of temperature with fluctuation-assisted tunneling theory fit. In order to convert to resistivity, the formula $\rho = R \cdot 2.8 \times 10^{-3} \text{ m}$ can be used. (b) Thermistor sensitivity figures of merit, calculated from a 10 term polynomial fit (not shown). At 4 K, the VACNT $\text{TCR} = -0.3 \text{ K}^{-1}$ and $\alpha = -1.2$.

shown in figure 6 to account for unknown deviations from our assumptions.

We note that it is possible to further reduce the VACNT reflectance by exposure to oxygen plasma (ashing) [8]. After ashing for 15 s at 200 W, the witness chip THR was reduced by 40% at 1550 nm. However, the PBR discussed in this paper was not ashed.

5. Thermistor

The measured VACNT thermistor resistance (R) as a function of temperature (T) fits well to fluctuation-assisted tunneling theory [14] with an additional linear term for the change in Mo lead resistance at high temperatures given by $R = A \exp(T_1 / (T + T_2)) + BT$, with fit parameters $A = 45.21 \text{ } \Omega$, $T_1 = 17.11 \text{ K}$, $T_2 = 4.12 \text{ K}$ and $B = 0.2 \text{ } \Omega \text{ K}^{-1}$ (figure 7(a)). Figure 7(b) shows two common thermistor sensitivity figures of merit, temperature coefficient of resistance ($\text{TCR} = 1/R \cdot dR/dT$) and $\alpha = T/R \cdot dR/dT$.

6. Heater

Due to an unexpected elevation of the Mo superconducting critical temperature (T_c) to 3.884 K (figure 8(a)), we are limited to operating temperatures above T_c where the Mo is normal ($R_n = 74.5 \text{ } \Omega$) and the electrical heater dissipates heat. Since Mo usually has a T_c below 1 K, we speculate that the VACNT growth modifies the Mo, possibly forming molybdenum carbide. On separate devices, we have measured T_c values up to 7 K. The elevated T_c opens the possibility for future devices to use the Mo as an extremely sensitive thermistor (figure 8(b)) operating as a transition-edge sensor (TES). Additionally, Mo traces could be used for thin-film superconducting wiring instead of Al wirebonds.

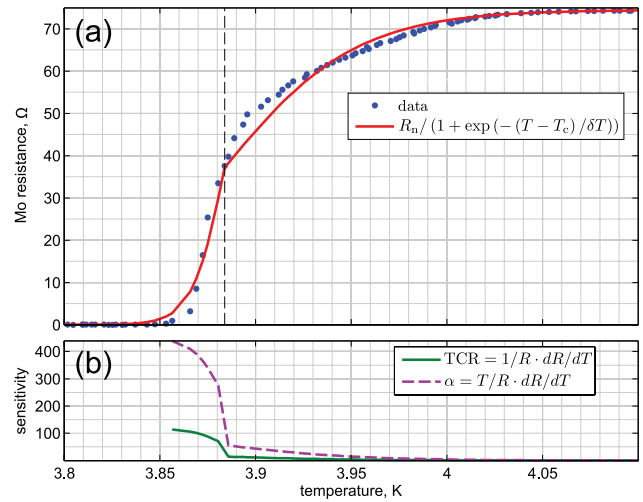


Figure 8. (a) Mo heater resistance as a function of temperature with logistic function fit $R = R_n / (1 + \exp(-(T - T_c) / \delta T))$. Since the transition is not symmetric about T_c , we fit for different values of δT below T_c ($\delta T = 8.4 \text{ mK}$) and above T_c ($\delta T = 34.4 \text{ mK}$). The dashed vertical line shows T_c . In order to convert to resistivity, the formula $\rho = R \cdot 2.5 \times 10^{-9} \text{ m}$ can be used. (b) Thermistor sensitivity figures of merit, calculated from fits. At T_c , the Mo $\text{TCR} = 14.1 \text{ K}^{-1}$ and $\alpha = 54.9$.

7. Thermal modeling

By varying the applied electrical power (P_{elec}) from 1 μW to 800 μW and monitoring the thermistor temperature, we find that the thermal conductance (G) of the PBR is best fit by a cubic temperature dependence of $G = dP_{\text{elec}}/dT = G_0 T^3$, where G_0 is a constant. The integrated power law is then $P_{\text{elec}} = G_0 / 4 (T^4 - T_{\text{HS}}^4)$, where T_{HS} is the temperature of the heatsink. Solving for G_0 and using measured values of $P_{\text{elec}} = 131.15 \text{ } \mu\text{W}$, $T = 4.325 \text{ K}$ and $T_{\text{HS}} = 4.0772 \text{ K}$ gives $G_0 = 7.13 \text{ } \mu\text{W K}^{-4}$. This gives a thermal conductance at 4 K of $456 \text{ } \mu\text{W K}^{-1}$.

Using finite-element model (FEM) software, we have modeled the two dimensional (2D) temperature profile of the PBR. We have assumed the Si thermal conductivity is isotropic with a temperature dependence of $\kappa_{\text{Si}} = \kappa_{\text{Si},0} T^3$, where $\kappa_{\text{Si},0}$ is an unknown constant. For the conductivity of the Al wirebonds, we have assumed a linear temperature dependence of $\kappa_{\text{Al}} = \kappa_{\text{Al},0} T$ with $\kappa_{\text{Al},0} = 3 \text{ W m}^{-1} \text{ K}^{-2}$ [15]. Therefore, the power loss due to one Al wirebond is $P_{\text{Al},1} = 1/2(\kappa_{\text{Al}}/T \cdot A_{\text{Al}}/L_{\text{Al}})(T^2 - T_{\text{HS}}^2)$, where A_{Al} is the wirebond cross sectional area and L_{Al} is the wirebond length. The power loss due to blackbody radiation is $P_{\text{rad}} = A\sigma\epsilon(T^4 - T_{\text{HS}}^4)$, where A is the area, σ is the Stefan–Boltzmann constant and ϵ is the emissivity with $\epsilon_{\text{VACNT}} = 1$ and $\epsilon_{\text{Si}} = 0.1$ [5, 16]. The model required a value of $\kappa_{\text{Si},0} = 0.166 \text{ W m}^{-1} \text{ K}^{-4}$ in order to match the measured conditions of P_{elec} , T and T_{HS} listed above.

Figure 9(a) shows the modeled 2D FEM temperature profile for an applied power of 130 μW . Two cross section temperature profiles are shown in figure 9(b), which simulate an electrical substitution measurement. First, 130 μW of electrical power is applied without any optical power (dark), then 30 μW of electrical power and 100 μW of optical power

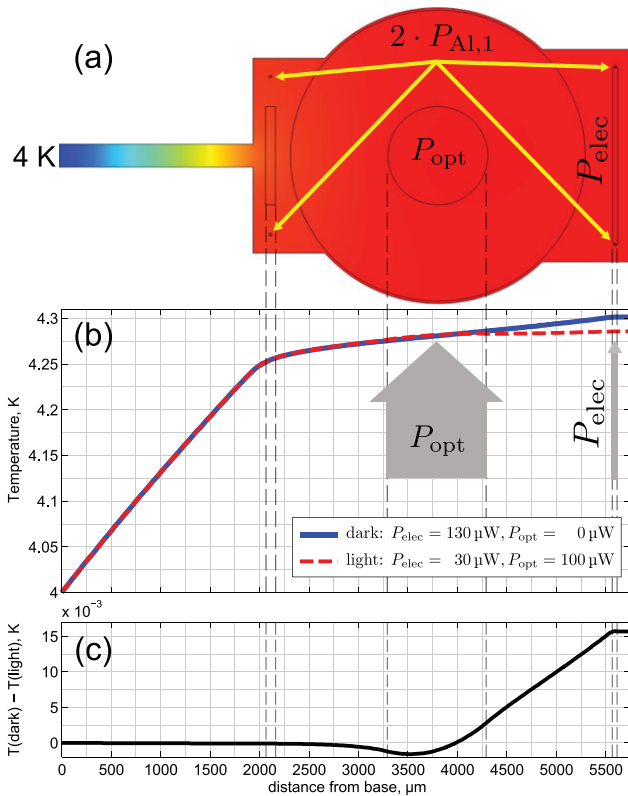


Figure 9. (a) Modeled 2D FEM temperature profile for 130 μW of applied power. Color legend not shown, see part (b) for temperatures. (b) 1D temperature profile along center of 2D FEM (part (a)) for two cases (dark and light) described in text. (c) Difference in temperature of two curves in part (b).

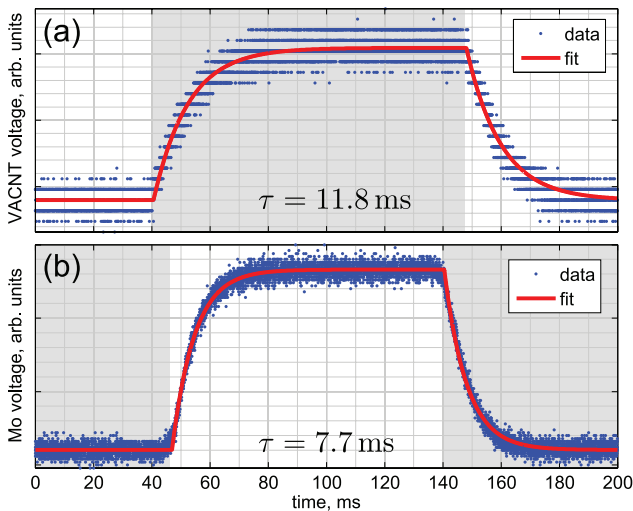


Figure 10. (a) VACNT at 4 K and (b) Mo at 3.884 K temporal response due to chopping the optical power ($\approx 102 \mu\text{W}$). The digitization in (a) is due to the low resolution of the oscilloscope. Shading indicates times when optical power is off.

(distributed evenly over a 1 mm diameter circle) is applied (light). For both cases, the modeled power loss due to the eight wirebonds is $\approx 2 \mu\text{W}$, while the power loss due to radiation is $\approx 40 \text{ pW}$. The mean temperature at the thermistor is 0.09 mK less for the dark case (figure 9(c)). In order to perfectly match the temperature at the thermistor for both cases, an additional

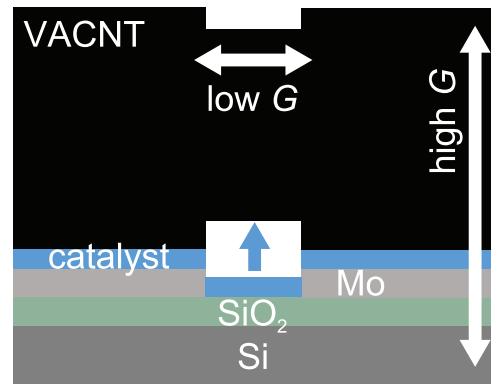


Figure 11. Schematic sectional view of thermistor VACNT showing VACNT pulled off substrate over SiO_2 . Thicknesses are not to scale.

power of 0.05 μW is needed for the dark electrical power. We use this modeled power difference in order to get a correction for the power inequivalence (δP_{equiv}).

8. Time constant

To find the time constant of the PBR, we used the optical switch to chop the optical power while monitoring the current-biased thermistor voltage on an oscilloscope. An exponential fit to the thermistor voltage signal yielded a time constant ($1/e$) of 11.8 ms at 4 K (figure 10(a)).

Due to the elevated T_c of the Mo, we were also able to regulate the heatsink temperature in the superconducting transition and monitor the current-biased Mo voltage. An exponential fit to the Mo voltage signal yielded a time constant ($1/e$) of 7.7 ms at 3.884 K (figure 10(b)).

We attribute the slower VACNT thermistor time constant to an additional weak thermal link. The thermistor behaves as if it is not well thermally coupled to the substrate, perhaps because the growth rate of the VACNT over Mo is higher than over SiO_2 (figure 11). The transverse VACNT thermal conductance (nanotube to nanotube) is orders of magnitude lower than the axial thermal conductance (nanotube to substrate) [17], which leads to a longer thermistor time constant.

9. Measuring optical fiber power

In order to measure the optical power leaving the fiber, the following steps are performed:

- (a) Optical switch to port 1 (power meter). (1 s)
- (b) Pause to stabilize power meter. (4 s)
- (c) Record power meter reading. (1 s)
- (d) Pause for temperature stabilization of PID loops. (44 s)
- (e) Record dark (optical power off) voltages. (2 s)
- (f) Optical switch to port 2 (PBR). (1 s)
- (g) Pause for temperature stabilization of PID loops. (44 s)
- (h) Record light (optical power on) voltages. (2 s)

These eight steps, which take a total time of 99 s, constitute two independent and traceable optical fiber power measurements:

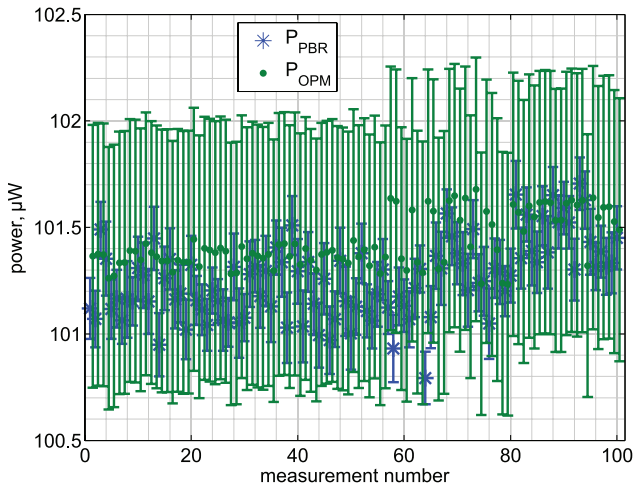


Figure 12. Results of 100 measurements of P_{PBR} and P_{PM} with uncertainty ($k = 2$) shown by error bars.

a PBR electrical-substitution measurement and a commercial power meter measurement.

$$P_{PBR} = (1 - R_{THR}) \cdot \left[\left(\frac{V_{ref,D} - V_{ref,D,0}}{R_{ref}} \right) \cdot (V_D - V_{D,0}) + \delta P_{equiv} - \left(\frac{V_{ref,L} - V_{ref,L,0}}{R_{ref}} \right) \cdot (V_L - V_{L,0}) \right] \quad (1)$$

The measurement equation for the PBR power measurement (P_{PBR}) is shown in equation (1). Line 1 is a correction for the non-unity VACNT absorption. Line 2 is the Joule power dissipated in the electrical heater with the optical power off (dark), where R_{ref} is the current reference resistor, $V_{ref,D}$ is the voltage across R_{ref} with offset voltage $V_{ref,D,0}$ and V_D is the voltage across the Mo heater with offset voltage $V_{D,0}$. The term δP_{equiv} is the offset power correction due to nonequivalence determined from the FEM. Line 3 is the Joule power dissipated in the electrical heater with the optical power on (light), where $V_{ref,L}$ is the voltage across R_{ref} with offset voltage $V_{ref,L,0}$ and V_L is the voltage across the Mo heater with offset voltage $V_{L,0}$.

$$P_{PM} = \left(\frac{P_1}{C_{abs} \cdot C_{NL}(P_1)} \cdot u_{pol} \right) \cdot r_{switch} \cdot u_{f,bend} \cdot \left(\frac{1 - \left| \frac{n_{vac} - n_{f,cold}}{n_{vac} + n_{f,cold}} \right|^2}{1 - \left| \frac{n_{air} - n_{f,warm}}{n_{air} + n_{f,warm}} \right|^2} \right) \quad (2)$$

The measurement equation for the commercial power meter (P_{PM}) is shown in equation (2). Line 1 applies NIST-calibrated correction factors to convert the power meter reading (P_1) into the actual optical power incident on the optical power meter. The absolute calibration factor C_{abs} is measured at 1549.6 nm and 100 μW [18]. The nonlinear correction factor $C_{NL}(P_1)$ corrects for power meter nonlinearities at other powers [19]. The variable $u_{pol} = 1$ adds an uncertainty (0.014%) due to the power meter dependence on polarization. Line 2 corrects

Table 1. Typical uncertainty budget for the PBR measurement equation (1). Values (uncertainties) shown are the mean value (uncertainty) of 100 measurements. For type A uncertainties, N is the number of measurements. When N is not listed, the uncertainty is the combined uncertainty ($k = 1$) from a separate measurement. For type B uncertainties, a uniform distribution has been assumed and the stated uncertainty has been divided by $\sqrt{3}$.

Variable	Value (x)	Uncertainty		
		Type/ N	Value (u_x)	% frac.
R_{THR}	0.00065	A/3	0.00025 ^a	0.025
V_D (V)	0.09890	A/10	0.00003	0.04
$V_{D,0}$ (μV)	0.5	A and B ^b	0.7	0.001
$V_{ref,D}$ (V)	1.3261	A/10	0.0004	0.04
$V_{ref,D,0}$ (μV)	48	A and B ^b	7	0.0007
δP_{equiv} (μW)	0.050	B	0.003	0.003
V_L (V)	0.04719	A/10	0.00003	0.018
$V_{L,0}$ (μV)	-0.7	A and B ^b	0.7	0.0004
$V_{ref,L}$ (V)	0.6329	A/10	0.0004	0.019
$V_{ref,L,0}$ (μV)	-6	A and B ^b	7	0.0003
R_{ref} (Ω)	999.994	A	0.007	0.0006
P_{PBR} (μW)	101.26			
Combined uncertainty (μW)			0.07	0.07
Expanded uncertainty (μW)			0.14	0.14

^a Value is double the measured value (figure 6) since the THR of the VACNT absorber was not measured directly or under operating conditions.

^b Voltage offsets are a combination of three measured offsets, of which, one is type A and two are type B.

Note: The last column (percent fractional uncertainty) is $\left| \frac{\partial P_{PBR}}{\partial x} \cdot \delta x \right| / P_{PBR} \cdot 100$. The expanded uncertainty is $k = 2$.

for the optical switch. With the cryostat open, the measured power out of the optical fibers on ports 1 and 2 are $P_{1,open}$ and $P_{2,open}$, respectively. The optical switch power ratio is $r_{switch} = P_{2,open}/P_{1,open}$. The variable $u_{f,bend} = 1$ adds an uncertainty (0.045%) due to the change in position of the fiber for the two measurements. Line 3 corrects for the difference in reflection from the port 2 fiber tip measured under conditions of atmospheric pressure at 294 K to the reflection under conditions of vacuum at 4.0772 K (a 0.01% correction). We have assumed Fresnel reflection at the face of the fiber tip where the index of refractions are $n_{vac} = 1$ for vacuum, n_{air} for atmospheric pressure, $n_{f,warm}$ for the fiber core at room temperature and $n_{f,cold}$ for the fiber core in the cryostat [20, 21].

With an applied optical power of $\approx 101.3 \mu W$, the eight measurement steps were repeated 100 times (figure 12). For each variable in the measurement equations, the mean value and mean uncertainty from the 100 measurements is listed in tables 1 and 2. The mean value and mean expanded uncertainty for both measurements of optical fiber power is:

- $P_{PBR} = 101.26 \mu W$ with an expanded uncertainty ($k = 2$) of 0.14 μW
- $P_{PM} = 101.43 \mu W$ with an expanded uncertainty ($k = 2$) of 0.62 μW

For these measurements, the heatsink was regulated at 4.0772 K and the PBR was regulated at 4.325 K ($R = 350 \Omega$). The mean of the 99 s standard deviation ($k = 2$) temperature fluctuations of the heatsink and PBR temperatures were 110 μK and 2.9 mK, respectively.

Table 2. Typical uncertainty budget for the optical power meter measurement equation (2). Values (uncertainties) shown are the mean value (uncertainty) of 100 measurements. For type A uncertainties, N is the number of measurements. When N is not listed, the uncertainty is the combined uncertainty ($k = 1$) from a separate measurement.

Variable	Value (x)	Uncertainty		
		Type/ N	Value (u_x)	% frac.
P_1 (μW)	96.3	A/1	0.1	0.12
C_{abs}	1.0058	A	0.0025	0.25
$C_{\text{NL}}(P_1)$	0.99999	A	0.00065	0.065
u_{pol}	1	B	0.00008	0.008
r_{switch}	1.059	A/4	0.001	0.1
$u_{f,\text{bend}}$	1	B	0.00026	0.026
n_{air}	1.0002	B	0.000001	0.00002
$n_{f,\text{cold}}$	1.443 10	A	0.00001	0.0001
$n_{f,\text{warm}}$	1.444 40	A	0.00001	0.0001
$P_{\text{PM}}(\mu\text{W})$	101.43			
Combined uncertainty (μW)			0.31	0.30
Expanded uncertainty (μW)			0.62	0.61

Note: The last column (percent fractional uncertainty) is $\left| \frac{\partial P_{\text{PM}}}{\partial x} u_x \right| / P_{\text{PM}} \cdot 100$. The expanded uncertainty is $k = 2$.

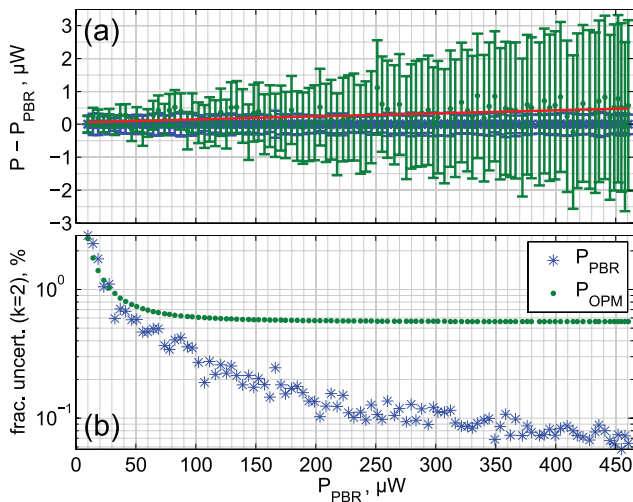


Figure 13. Results of 100 measurements of varying applied optical powers. (a) P_{PBR} has been subtracted purely for figure clarity and no error propagation was performed for the subtraction. The expanded uncertainty ($k = 2$) is shown by error bars. The solid red line is a linear fit to the P_{PM} offset with a slope of 0.0009. (b) Fractional uncertainty percentage versus power.

9.1. Linearity

As a check of linearity, the eight measurement steps were performed for 100 different applied optical powers from 10 μW to 460 μW (figure 13). From the FEM, we fit $\delta P_{\text{equiv}} = m \cdot P_1 + b$ where $m = 3.4 \times 10^{-4}$ and $b = 6.2 \text{ nW}$. A linear fit to the difference of $P_{\text{PM}} - P_{\text{PBR}}$ shows that P_{PM} is consistently higher than P_{PBR} by 0.09%. While this difference is within the combined uncertainties, it suggests that some of the uncertainties may be biased.

For the linearity measurements, the heatsink was regulated at 4.0776 K and the PBR was regulated at 4.8074 K ($R = 304 \Omega$). The mean of the 99 s standard deviation ($k = 2$)

temperature fluctuations of the heatsink and PBR temperatures were 1 mK and 4 mK, respectively.

10. Discussion

The main limitation of the current PBR measurements is the poor sensitivity of the VACNT thermistor, which leads to poor PID temperature stability. As a performance test, we swapped the roles of the VACNT thermistor and Mo heater to be VACNT heater and Mo thermistor. Since the Mo transition is much more sensitive than the VACNT, the PID temperature fluctuations of the PBR are 38 times lower. Additionally, the Mo was operated under a current bias, which is a positive electrothermal feedback mode. The temperature fluctuations would be even lower if operated under a voltage bias, which is a negative electrothermal feedback mode [22]. However, the PBR was not designed for operation in this swapped mode and the poor thermalization of the VACNT heater leads to measurements of P_{PBR} that are low (2.3% below P_{PM}), which we attribute to blackbody radiation from the hot VACNT heater coupling to the VACNT absorber.

By using a more sensitive voltage-biased Mo thermistor and a normal metal heater, the uncertainty of future PBR measurements should be limited only by the uncertainty in the measurement of the reflectance of the VACNT. In conclusion, we have demonstrated results of a lithographic electrical-substitution carbon nanotube radiometer. The lithographic design allows for greater flexibility and lower time constants, compared to traditional cryogenic radiometers. In addition to being a primary standard for optical power, by further decreasing the time constant and using high speed PID electronics, the PBR could find applications in Fourier transform infrared (FTIR) spectroscopy.

Acknowledgments

SEM image was taken by A Sanders in the Precision Imaging Facility at NIST Boulder.

References

- [1] Martin J E, Fox N P and Key P J 1985 *Metrologia* **21** 147
- [2] Carter A C, Woods S I, Carr S M, Jung T M and Datla R U 2009 *Metrologia* **46** S146
- [3] Livigni D J, Tomlin N A, Cromer C L and Lehman J H 2012 *Metrologia* **49** S93
- [4] Yang Z, Ci L, Bur J A, Lin S and Ajayan P M 2008 *Nano Lett.* **8** 446–51
- [5] Mizuno K, Ishii J, Kishida H, Hayamizu Y, Yasuda S, Futaba D N, Yumura M and Hata K 2009 *Proc. Natl Acad. Sci.* **106** 6044–7
- [6] Lehman J, Sanders A, Hanssen L, Wilthan B, Zeng J and Jensen C 2010 *Nano Lett.* **10** 3261–6
- [7] Chunnillall C J, Lehman J H, Theocharous E and Sanders A 2012 *Carbon* **50** 5348–50
- [8] Tomlin N, Curtin A, White M and Lehman J 2014 *Carbon* **74** 329–32
- [9] Carter A, Datla R, Woods S and Jung T 2008 *Proc. SPIE:* **7021** 70210S
- [10] Tomlin N A and Lehman J H 2013 *Opt. Lett.* **38** 175–7

- [11] Jiang Y Q, Zhou Q and Lin L 2009 *IEEE 22nd Int. Conf. MEMS* pp 587–90
- [12] Jiang Y, Wang P and Lin L 2011 *Nanotechnology* **22** 365704
- [13] Kowalevich A M and Bucholtz F 2006 *Technical Report NRL/MR/5650-06-8996* Naval Research Laboratory (www.dtic.mil/docs/citations/ADA456331)
- [14] Kaiser A B, Skakalova A V and Roth S 2008 *Physica E* **40** 2311
- [15] Woodcraft A L 2005 *Cryogenics* **45** 421–31
- [16] Mowla L 2013 Radiative cooling of silicon mirror for gravity wave detection *Honors Thesis* Wellesley College, USA (<http://repository.wellesley.edu/thesiscollection/154>)
- [17] Berber S, Kwon Y K and Tománek D 2000 *Phys. Rev. Lett.* **84** 4613–6
- [18] Vayshenker I, Li X, Livigni D, Scott T and Cromer C L 2000 *NIST Special Publication* pp 250–54 (www.nist.gov/calibrations/upload/sp250-54.pdf)
- [19] Vayshenker I, Yang S, Li X, Scott T and Cromer C L 2000 *NIST Special Publication* pp250–56 (www.nist.gov/calibrations/upload/sp250-56-2.pdf)
- [20] Ciddor P E 1996 *Appl. Opt.* **35** 1566–73
- [21] Leviton D B and Frey B J 2006 *Proc. SPIE* **6273** 62732k vol 6273, ed D Lemke et al (Washington, DC: SPIE)
- [22] Irwin K D 1995 *Appl. Phys. Lett.* **66** 1998–2000